Radiation therapy effects on white matter fiber tracts of the limbic circuit

Mohammad-Reza Nazem-Zadeh,[a] Christopher H. Chapman,[b] Theodore L. Lawrence,[c] and Christina I. Tsien[d]
Department of Radiation Oncology, University of Michigan, Ann Arbor, Michigan 48109-0010

Yue Cao[e]
Departments of Radiation Oncology, Radiology, and Biomedical Enegeneering, University of Michigan, Ann Arbor, Michigan 48109-0010

(Received 24 February 2012; revised 25 July 2012; accepted for publication 25 July 2012; published 24 August 2012)

Purpose: To segment fiber tracts in the limbic circuit and to assess their sensitivity to radiation therapy (RT).
Methods: Twelve patients with brain metastases who had received fractionated whole brain radiation therapy to 30 Gy or 37.5 Gy were included in the study. Diffusion weighted images were acquired pre-RT, at the end of RT, and 1-month post-RT. The fornix, corpus callosum, and cingulum were extracted from diffusion weighted images by combining fiber tracking and segmentation methods based upon characteristics of the fiber bundles. Cingulum was segmented by a seed-based tractography, fornix by a region of interests (ROI)-based tractography, and corpus callosum by a level-set segmentation algorithm. The radiation-induced longitudinal changes of diffusion indices of the structures were evaluated.
Results: Significant decreases were observed in the fractional anisotropy of the posterior part of the cingulum, fornix, and corpus callosum from pre-RT to end of RT by –14.0%, –12.5%, and –5.2%, respectively ($p < 0.001$), and from pre-RT to 1-month post-RT by –11.9%, –12.8%, and –6.4%, respectively ($p < 0.001$). Moreover, significant increases were observed in the mean diffusivity of the corpus callosum and the posterior part of the cingulum from pre-RT to end of RT by 6.8% and 6.5%, respectively, and from pre-RT to 1-month post-RT by 8.5% and 6.3%, respectively. The increase in the radial diffusivity primarily contributed to the significant decrease in the fractional anisotropy, indicating that demyelination is the predominant radiation effect on the white matter structures.
Conclusions: Our findings indicate that the fornix and the posterior part of the cingulum are significantly susceptible to radiation damage. We have developed robust computer-aided semiautomatic segmentation and fiber tracking tools to facilitate the ROI delineation of critical structures, which is important for assessment of radiation damage in a longitudinal fashion. [http://dx.doi.org/10.1118/1.4745560]

Key words: whole brain radiation therapy, metastases, segmentation, limbic circuit fiber tracts, radiation sensitivity, cingulum, fornix, corpus callosum

I. INTRODUCTION

The assessment of various radiation-induced effects on important white matter tracts in the central nervous system may aid in reducing toxicity by guiding radiation delivery and avoiding regions at high risk for damage.[1–6] Although some fiber tracts have been longitudinally assessed for radiation-induced structural changes, most previous assessments have been carried out only on a limited portion of fiber tracts of interest[7–10] which do not reflect the characteristics of the entire structure. The limbic circuit fiber tracts, including fornix (projected from hippocampus to the septal region and mamillary bodies connecting the hippocampal formation to the hypothalamus) and cingulum (connecting the cingulate and the parahippocampal gyri to the enthorinal cortex), play a major role in emotional association functions with memory.[11] A previous study of cognitive dysfunction shows the hippocampus and the anatomically related cortex sensitivity to radiation.[12] However, a quantitative analysis on the radiation sensitivity of white matter structures in the limbic circuit has not been prospectively conducted.

Diffusion weighted magnetic resonance imaging (DW-MRI) is a highly sensitive modality for evaluating damage to the microstructure of white matter tracts, which is not visible on any other conventional images. Extracting various fiber tracts from diffusion weighted images (DWIs) makes it possible to quantify their diffusion characteristics and thus monitor the therapy side effects on them. In order to accurately assess the radiation effects on each white matter structure through the diffusion indices, it is important to precisely and reproducibly delineate the fiber tract boundaries. Manual delineation of the desired fiber tract in slices covering the whole structure is time-consuming, as it requires the operator's neuro-anatomic knowledge about the fiber tract of interest. Moreover, errors may be introduced into the manually delineated contours, particularly when the fiber structure size varies across the 2D image slices. Another commonly used approach is to track fiber bundles (tractography) through

manually defined regions of interests (ROIs) and extract the outer boundaries of the whole structure. Previous studies have shown that it is challenging to delineate the whole cingulum, especially its anterior and descending posterior parts, if the number of ROIs and their locations are not adequately selected.[9,13,14] Moreover, placing ROIs with a large separation between them leads in discontinuity in the extracted cingulum fibers and creates wrong fiber trajectories in between, which must eventually be pruned. In a previous study, probabilistic tractography was used to segment the cingulum, in which a limited number of seed points are inserted and then 3×3-voxels ROIs are created around the seeds.[15] Because local thickness changes throughout the cingulum, the fixed ROI size around the seed points is not a realistic consideration of the tract cross section, and this approach leads to under/overestimation of the cingulum thickness. In a nonparametric segmentation framework that is proposed based on tensor coherence in Riemannian manifolds, although the cingulum fiber tract is extracted, the method is not capable of catching the posterior part of the cingulum.[16] Another attempt to segment the cingulum is to use a tubular model,[17] in which the segmentation problem is reduced to a parametric estimation of centerline and radius function, which leads to an erroneous estimation in the cingulum, especially in the anterior part, due to its variation in the radius along the fiber bundle. Although other methods have been proposed for high angular resolution diffusion imaging (HARDI) data, they are not applicable for diffusion tensor imaging (DTI) data[18–21] as they rely on more than one principal diffusion direction which is not achievable using DTI data. Finally, to extract the fornix, although tractography with ROI insertion has been attempted, the extracted structure is either incomplete[22] or expanded outside of the fornix.[23]

In this paper, our goal is to study the effects of radiation on limbic circuit fiber tracts using DTI. We propose a seed-based multi-ROI tractography algorithm for segmenting the entire cingulum, in which the coronal or axial ROIs for tractography are automatically created from the seeded points by the proposed level-set segmentation framework. Next, a new appropriate multi-ROIs depiction is suggested for the tractography of the fornix fiber tract. Finally, the corpus callosum, the largest white matter fiber bundle in the brain, is segmented by level-set segmentation. After segmenting the cingulum, fornix and corpus callosum, we study the longitudinal changes in diffusion indices of these white matter structures from pre-RT (radiation therapy) to post-RT and investigate whether radiation affects these structures differently.

II. MATERIALS AND METHODS

II.A. Human subjects and image acquisition

Twenty-four patients who had brain metastases and received fractionated whole brain RT (WBRT) (30 Gy or 37.5 Gy) were prospectively enrolled in a DTI study. Twelve patients were chosen (six males, six females; mean age 53.5 years), who neither had severe edema or mass effect in white matter regions of interest, nor an insufficient number of slices covering the whole brain, nor head movements causing severe image distortion that cannot be compensated by image coregistration. DWIs were acquired on a 3T scanner MRI (Achieva, Phillips, Netherlands) pre-RT, at the end of RT (end-RT), and 1-month post-RT. DWIs along 15 different diffusion gradient directions (with b-value $= 1000$ s/mm^2) plus a b_0 reference image (with b-value $= 0$) were collected with a voxel size of $1.75 \times 1.75 \times 2$ mm^3 to cover the whole brain.

II.B. Data preprocessing

Before segmenting the white matter fiber bundles of interest, the diffusion weighted images were prepared through registration, interpolation, denoising, gradient correction, and tensor calculation.

II.B.1. Intra- and interseries coregistration

For eliminating the image distortion caused by patient movements and MRI hardware-induced drafts within image volumes, DWIs in a series were registered to the corresponding b_0 image by using mutual information and the affine transform. For comparing each patient's images across time points, all series were coregistered to pre-RT images.

II.B.2. Interpolation

As it is preferable to have the same step size in all directions for the front propagation in the level-set segmentation algorithm (description given in Sec. II.C.1.b), the images were interpolated to an isotropic voxel size of $1.75 \times 1.75 \times 1.75$ mm^3 by up-sampling the data in the interslice direction.

II.B.3. Denoising

The acquired DWI images usually suffer from low signal-to-noise ratio which affects the results of any segmentation or fiber tracking algorithm. Without prolonging the image acquisition, we applied the anisotropic diffusion filter with proven advantages over Gaussian kernels for the MRI images.[24,25] For our specific dataset, we set the anisotropic filtering parameters as: 1000 for the gradient modulus threshold in controlling the conduction in 26 neighboring nodes and 3/44 for the integration constant in meeting numerical stability.[24] We used the smoothed DWIs for fiber tract boundary segmentation. However, the original nonsmoothed DWIs were used for assessing radiation effects.

II.B.4. Gradient table correction

The diffusion gradients on the Philips MRI system are given in the physical coordinate system, while DWIs are reconstructed in the image coordinate system. Therefore, the gradient table was recalculated in the image coordinate system by using the image orientation prescribed in the Dicom Header of the DWI slices.

II.B.5. Calculation of tensor and diffusion indices

Using the corrected diffusion table, the diffusion tensor, fractional anisotropy (FA), mean diffusivity (MD), radial diffusivity (RD) (the mean of the two smaller eigen values of the tensor), and axial diffusivity (AD) (the largest eigen value of the tensor) of each voxel, along with the principal diffusion direction (PDD) (the eigen vector corresponding to the largest eigen value of the tensor) were calculated.

II.C. Segmentation of fiber tracts

We adopted different strategies for segmenting the corpus callosum, cingulum, and fornix.

II.C.1. Cingulum segmentation

To segment the whole structure of the cingulum with local bundle thickness variation and possible disruptions through a ROI-based tractography, multiple ROIs must be inserted close together. However, depiction of the structure boundaries for a large number of ROIs is time consuming and sometimes inaccurate due to visual inspection. Therefore, we proposed a seed-based, robust, and reproducible tractography algorithm for segmenting the cingulum. Based on the location of the processed seed points (which will be introduced in Sec. II.C.1.b), a decision was made whether an axial or coronal ROI *was* more appropriate. Then, the axial/coronal ROIs were automatically extracted. Finally fiber tracking was performed.

II.C.1.a. Seed points processing. Using a clustering scheme, we separated and tagged the roughly 20 operator-inserted seed points on sagittal planes [Fig. 1(a)] into the left and right sides. Then, for each side, we sorted the seed points into a consecutive order from anterior to posterior. Furthermore, considering the sorted seed points as scattered points, a medial line was extracted for each side followed by a s*pline* fitting. The points sampled from the extracted s*pline* were named *processed* seed points.

II.C.1.b. Selection of coronal or axial ROI. 3D tractography is not capable of reconstructing the entire structure if performed between ROIs that form a large angle with the cross sections of the fiber bundle. The cingulum cross sections in the superior and inferior parts are usually more aligned with the coronal plane and in the anterior and posterior parts are usually more aligned with the axial plane. Therefore, depending on the location of the seed point, a ROI was extracted in a coronal or axial plane.

II.C.1.c. Automatic ROI extraction. After tagging the processed seed points for a coronal/axial ROI, we segmented 2D cross section ROIs of the cingulum using a level-set segmentation algorithm. A surface, defining the initial boundary of the structure, propagates in the direction normal to the surface, where a high level of similarity exists among diffusion indices, until reaching the outer boundary of the structure of interest. A level-set algorithm simplifies the calculation of geometric quantities such as normal to surface and

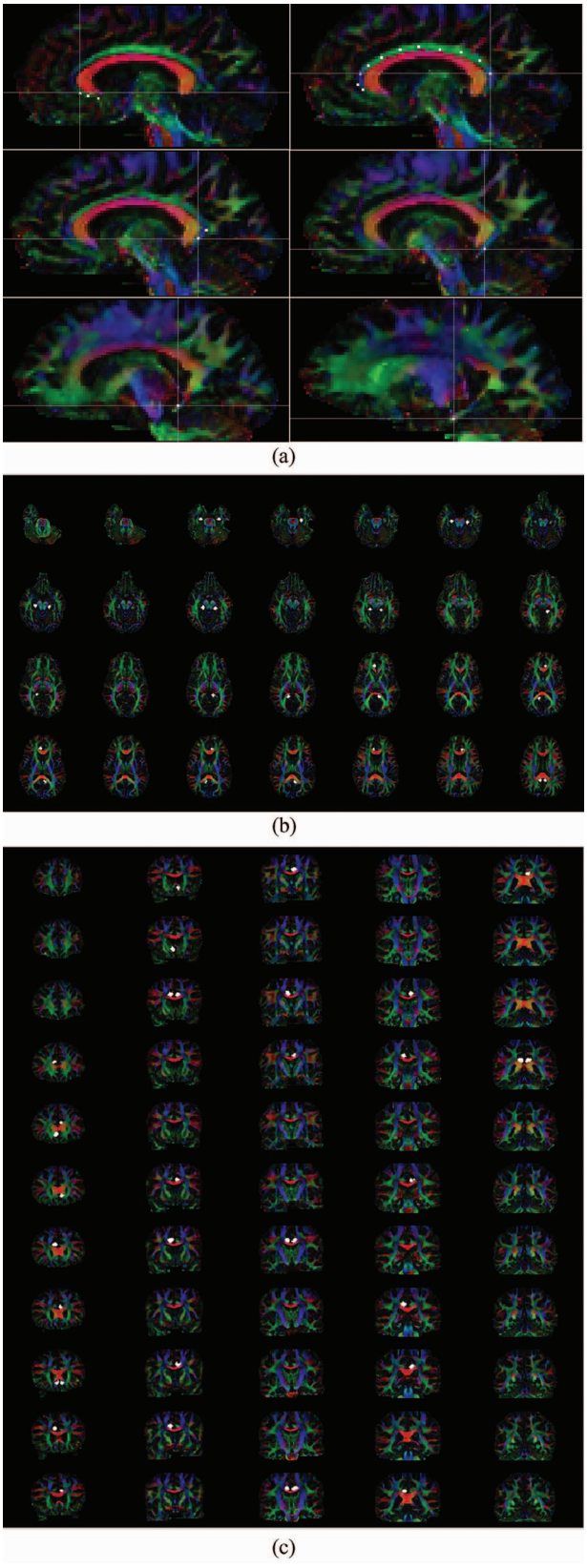

FIG. 1. (a) Inserting the seed points on different sagittal planes covering the cingulum in order to extract the appropriate ROIs for fiber tracking. (b) Axial views of the automatic segmentation results for the axial cross sections of the cingulum at the processed seed points in superior and inferior parts. (c) Coronal views of the automatic segmentation results for the coronal cross section of the cingulum at the processed seed points in anterior and posterior parts.

curvature.[26,27] The Hamilton-Jacobi partial differential equation in our application is reduced to

$$D_t\varphi(r,t) + F(r,t)||\nabla\varphi(r,t)|| = 0, \quad (1)$$

where $r \in R^n$ is the variable of state space R^n, φ: $R^n \times R \rightarrow R$ is the level-set function, $\nabla\varphi = D_r\varphi$ is the gradient of φ with respect to the state space variables, $D_t\varphi$ is the partial derivative of φ with respect to the time variable t, and $F(r,t)$ is the speed in the direction of normal to the surface. We used the level set toolbox developed by Ian M. Mitchell[28] as the core and changed the codes dramatically to fit to our application. The 5th order of the upwind method was used to calculate the first order spatial partial derivative $\nabla\varphi(r,t)$.[27]

Between each voxel on the 2D coronal/axial propagating curve and its neighbors in the propagation direction, we defined a similarity measure based on tensors, anisotropies, and principal diffusion directions (PDD) and used that as the speed term in the level-set framework. The speed term was thresholded by F_Thre to diminish the minor speed terms which might cause instability in the level-set framework. Since the cingulum and some of its neighboring structures such as the corpus callosum have nearly orthogonal diffusion directions, we used a threshold on the collinearity of PDDs (Colli_Thre) between the neighbor voxels to keep the propagating front inside the cingulum. Since the direction of the first diffusivity in the cingulum is almost perpendicular to the cross section of the structure, we considered the thresholds PDD_y_Thre on the PDD y-component [$PDD_y(r)$] and PDD_z_Thre on the PDD z-component [$PDD_z(r)$] to further prevent the front from propagating into neighbor structures in the coronal and axial ROIs, respectively. Another threshold FA_Thre was also used to prevent penetration of the cingulum boundary into neighboring structures with very low FA values.

The proposed segmentation steps for the cingulum are depicted in a flowchart in Fig. 2. To segment the coronal and axial cross sections (with high sensitivity of the estimation) without propagating the front into irrelevant adjacent fiber structures (with high specificity of the estimation) a set of the threshold values were chosen as: FA_Thre = 0.05, Colli_Thre = 0.5, F_Thre = 0.05, PDD_y_Thre = 0.8, and PDD_z_Thre = 0.8.

II.C.1.d. Tractography. Having the extracted multiple ROIs, we performed FACT (fiber assignment by continuous tracking) tractography[29] advancing through the entire cingulum.[29] In order to ensure to track more fibers to cover the entire structure and the proper local thickness, we run tractography between *every* pair *within* four consecutive ROIs. Then, in order to obtain segmentation results, we projected the fiber tract trajectories to the image volume.

II.C.1.e. Morphological post-processing. Due to low signal-to-noise ratio, low spatial resolution of the DWI images and the fibers crossing each other, a low FA value may lead to thinning or disruption in some parts of the extracted cingulum fiber bundle. For radiation-sensitivity evaluation purposes, a connected segment of the cingulum is needed, thus we post-processed the segmentation results through 3D morphological operations. The processed seed points were added to the segmented structure. Then, in order to fill any small hole in the structure body and make a smoother segment, a closing operation (a dilation followed by an erosion) was performed using a cubical structuring element with $2 \times 3 \times 3$ voxels. By adding processed seed points to the structure, the closing operation can reconstruct the thin or disconnected area and unify the segments to a connected smoothed structure. Such a morphological operation allows the smooth parts to remain unchanged and the average dimensions of the structure to remain close to its original. Using the highest curvatures on the fitted spline curve of the processed seed points, where the superior portion connects to the anterior and posterior parts, we divided each of the left and right cingulum bundles into three anterior, superior, and posterior parts.

II.C.2. Segmentation of fornix

For segmenting the fornix, we performed FACT tractography using multiple ROIs to segment this fiber tract.[29] For routing the fibers, multiple ROIs including three coronal ROIs on the body, one axial ROI at the most posterior part, and one terminating axial ROI at the inferior part of the fornix were used (Fig. 3). For reconstructing the most possible fibers, tractography between *every* pair of five *mentioned* ROIs were performed. We applied the pre-RT depicted ROIs to the coregistered images acquired at other time points and revised them, if needed. After performing tractography to each of time samples, we projected the fiber trajectories to the image volume to obtain the fornix segments for the time points. We defined *the majority counted tract* by majority counting between the segmentation results of all time samples. We labeled each voxel in the image volume on the *majority counted tract* if the majority of time samples encounter that voxel. If a patient *had more* time samples (at 3 or 6-month post-RT), we *included them all in* reconstruction of the *majority counted tract*, but we evaluated the indices *only* for the first three time samples.

II.C.3. Segmentation of corpus callosum

We segmented the corpus callosum using the level-set algorithm introduced before,[31] based on local tensor similarities measured between the neighbor voxels of a growing surface boundary. Using the tensor dissimilarity between the neighbor voxels would prevent the surface from propagating into adjacent white matter structures such as the cingulum, tapetum, minor and major forceps, and corticospinal fiber tracts. Since there is a smooth and gradual transition in shape and direction of the tensors from the corpus callosum to the minor and major forceps, which may cause a wrong penetration, we coded the specific diffusion pattern of the corpus callosum as a priori to obtain a high level of specificity for the segmentation.

II.D. Evaluation of reproducibility of the segmentation algorithms

To test the reproducibility of the proposed segmentation algorithm, test–retest diffusion tensor datasets of 12 patients

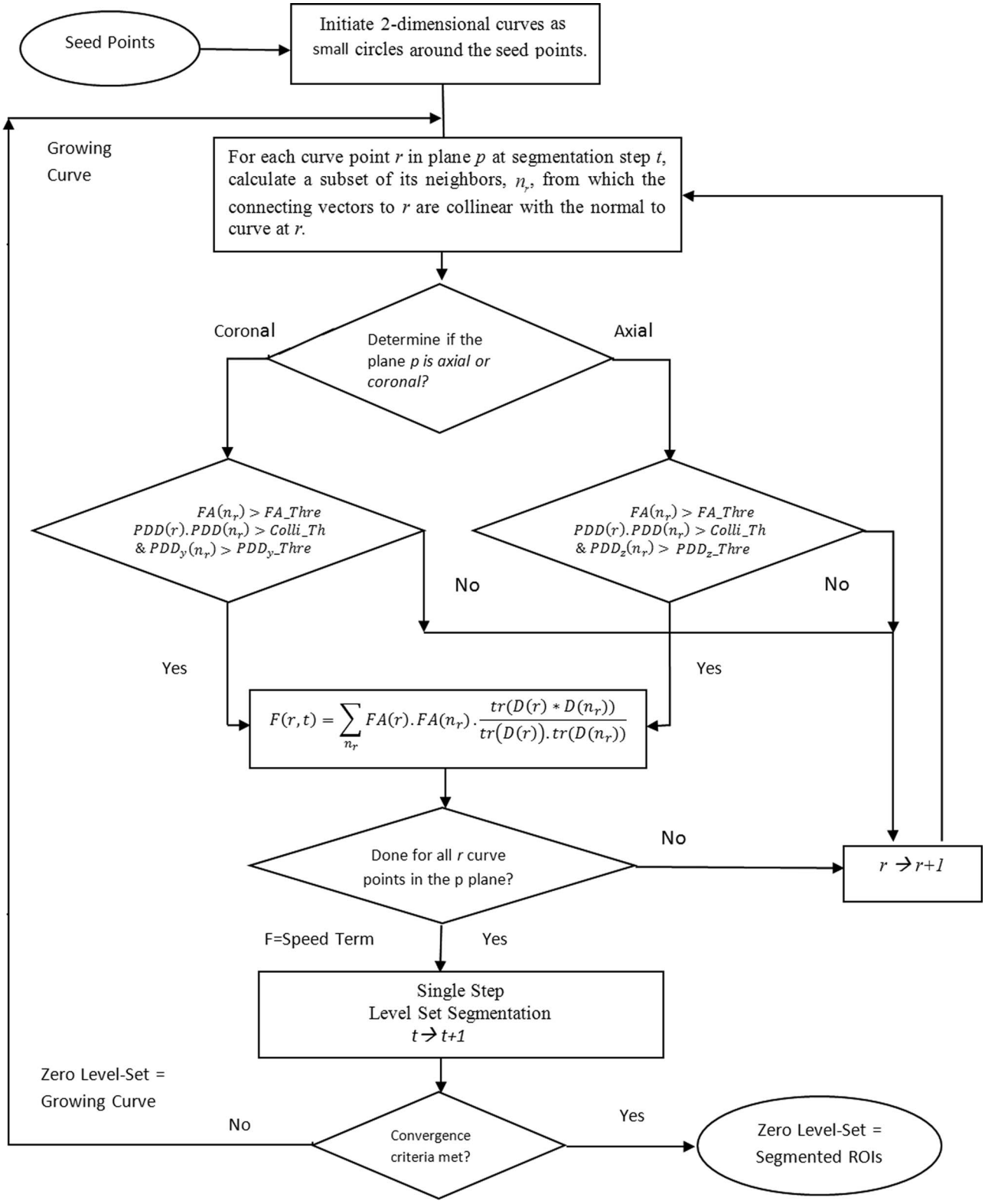

FIG. 2. The flowchart of the proposed algorithm for extracting ROIs from the initial seed points. *tr(.)* is the matrix trace and *D(r)* is the tensor calculated at point *r*.

were chosen from the NATIONAL BIOMEDICAL IMAGING ARCHIVE (NBIA) database. The DWIs were acquired on a 3T MRI (Siemens, Germany) using 12 diffusion gradient directions and a b_0 reference image with a matrix of 128 $\times$ 128 and a voxel size of 1.71 $\times$ 1.71 $\times$ 5 mm^3. We applied the same preprocessing procedures (except for the gradient table correction) and the proposed algorithm to both the test and retest datasets to segment the cingulum, and calculated the

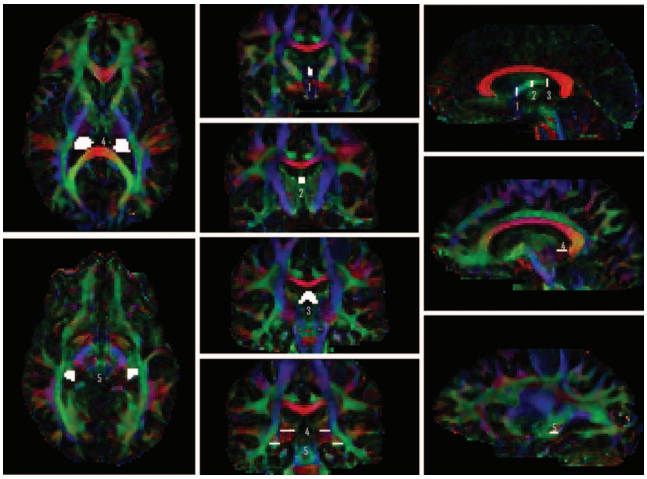

FIG. 3. Locations of multiple ROIs for the fornix fiber tracking; including three coronal ROIs on the body (labeled by 1, 2, and 3), an axial ROI at the most posterior part (labeled by 4), and a terminating axial ROI at the inferior part (labeled by 5).

Dice coefficient to measure the volumetric overlap between the segmented structures from the test and retest data. Also, to measure the level of uncertainty of the diffusion indices, we calculated the within-subject standard deviation for relative FA and MD (normalized by the means of the test and retest measures) in different cingulum segments, and repeatability coefficient (RC) to determine the 95% confidence interval (CI).[30]

II.E. Assessing the changes in diffusion indices after irradiation

We specified eight different structures, including six different parts of the cingulum (left and right posterior, superior, and anterior), fornix and corpus callosum. For the cingulum and corpus callosum, we extracted the shared area between the segments of all time samples and confirmed the shared volume to be a connected area for each of the patients. For the fornix, since the shared area in most cases was not smooth and connected, *the majority counted tract* was extracted and used to investigate the changes in diffusion indices after irradiation.

After verifying the histogram of diffusion indices as near to a normal distribution, we evaluated whether there were significant percentage changes in the diffusion indices of the segmented structures from pre-RT to the end of RT and from pre-RT to 1-month post-RT by paired t-test. Furthermore, we evaluated whether the changes in the different structures were the same after receiving the same radiation doses. After verifying insignificant differences in percentage changes between the cingulum's right and left sides, we combined the left and right anterior, superior, and posterior parts of the cingulum. Since it required ten comparisons for five structures (three cingulum parts, the fornix, and the corpus callosum) at two time points, a p-value less than $0.05/10 = 0.005$ was considered as significant.

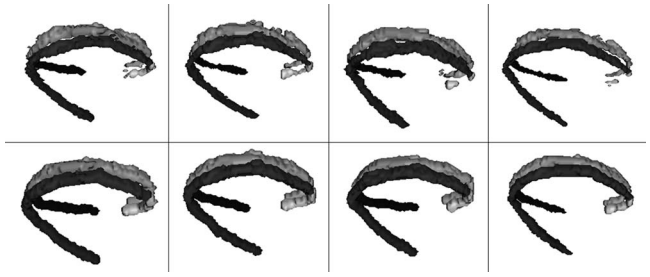

FIG. 4. The segmentation (top row) and the morphological operation (bottom row) results of the cingulum of a patient pre-RT (left), end-RT (second left), 1-month post-RT (second right), and the shared area between them (right).

III. RESULTS

First, we assessed the segmented fiber bundle structures, and the reproducibility of the segmentation. Then, we evaluated longitudinal changes in the DTI indices of the structures.

III.A. Segmented white matter structures

III.A.1. Cingulum

Figure 1(b) shows the axial views of the automatic segmentation ROIs for the axial cross section of the cingulum at the processed seed points in the anterior and posterior parts. Figure 1(c) represents the coronal views of the automatic segmentation ROIs for the coronal cross section of the cingulum at the processed seed points in the superior and inferior parts. Figure 4 shows the surface renditions of the segmented cingulum fiber bundles of one patient at three time points after fiber tracking alone and after applying the morphological operation. The shared area between the segments of all time points resembles each of the individual time samples and will be used in statistical analysis of the changes in diffusion indices (Fig. 4).

III.A.2. Fornix

Figure 5 displays the tractography and the segmentation results of a patient, along with the shared area, and *the majority counted tract* of different time samples. Note that *the majority counted tract* is fully connected, and much smoother than the shared and the individual segments. Figure 6 shows the segmented cingulum, fornix, and corpus callosum by the proposed methods of one patient in different views.

III.B. Reproducibility and evaluation of the proposed algorithm

We evaluated the reproducibility of the segmented cingulum by our proposed method using the test–retest data of the 12 patients from the NBIA database. The Dice coefficients of segmented structures, the within-subject standard deviation of the relative FA and MD, and RC between the test and retest data are given in Table I. The RCs that define the 95% CI of a parameter ranged from 0.0375 to 0.1510 for FA and from 0.0258 to 0.0432 for MD, suggesting any change that is

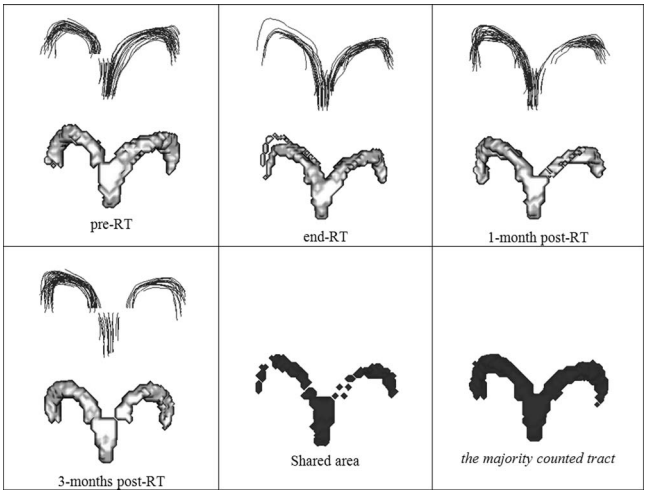

FIG. 5. The fiber tracking and the segmentation results for one patient with four time samples. The graphs in the middle and the right of the bottom row show the shared, and *the majority counted tract* between the segmentation results of different time samples, respectively. Note that *the majority counted tract* is quite smooth, and connected, compared to the shared and the individual segments with some disconnections.

greater than RC or less than –RC is beyond the uncertainty of test and retest [30] (Table I).

To further evaluate the performance of the proposed method, we compared the segmented cingulum by our method with one by the tractography followed by the ROIs insertion method reported by Wakana *et al.*,[14] which is shown in Fig. 7. Note that Wakana's method *reconstructed* a small number of fibers and thus *underestimated* the structure cross section. In addition, it did not reconstruct the left and right posterior parts of the cingulum.

III.C. Experimental results

III.C.1. Longitudinal percentage changes in diffusion indices

The mean FA and MD were examined in the extracted structures of the cingulum posterior, superior, and anterior parts, the fornix, and the corpus callosum of the 12 patients for the longitudinal percentage changes from pre-RT to end-RT and from pre-RT to 1-month post-RT (Table II). Compared to pre-RT, significant decreases in the mean FA were observed in the cingulum posterior part, fornix, and the corpus callosum by respectively –14.0%, –12.5%, and –5.2% at the end of RT; and by respectively –11.9%, –12.8%,

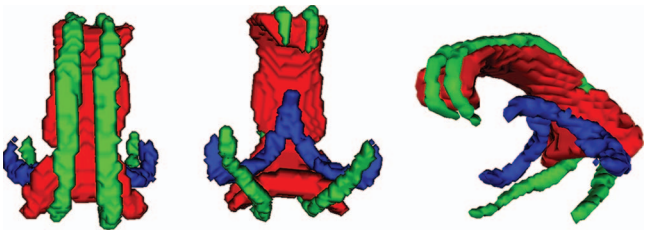

FIG. 6. Segmented cingulum, fornix, and corpus callosum of a patient by the proposed methods in different views.

TABLE I. The Dice coefficient of cingulum segments between the test and retest data, the unbiased estimate of within-subject standard deviation (SDw) and the related reproducibility coefficient (RC) for FA and MD in different cingulum segments.

	Posterior right	Superior right	Anterior right	Posterior left	Superior left	Anterior left
Dice Coefficient	0.926	0.951	0.878	0.929	0.954	0.899
SDw (FA)	0.0135	0.0229	0.0545	0.0227	0.0235	0.0361
SDw (MD)	0.0156	0.0110	0.0124	0.0125	0.0108	0.0093
RC (FA)	0.0375	0.0635	0.1510	0.0629	0.0651	0.1000
RC (MD)	0.0432	0.0304	0.0343	0.0346	0.0299	0.0258

and –6.4% 1-month post-RT ($p < 0.001$). A similar trend, but to a much smaller extent, was observed in the cingulum anterior and superior parts (from –3.1% to –6.6%) but did not reach the significant level after justifying the multiple comparison (Table II). Furthermore, compared to pre-RT, significant increases in the mean MD were observed in the corpus callosum and cingulum posterior part by 6.8% and 6.5% ($p < 0.001$) respectively at the end of RT and by 8.5% and 6.3% ($p < 0.0001$ and $p < 0.008$) respectively 1-month post-RT. In the remaining structures, there were no significant changes in the mean MD either at the end of RT or 1-month post-RT. Compared to the repeatability coefficients obtained in the test and retest data, the significant changes in FA and MD of the cingulum posterior part were beyond the 95% CI of the indices, which asserts the high level of certainty about the significance of the changes after brain irradiation.

To further reveal which diffusivity components contribute to the significant decreases in the FA in the cingulum posterior part, the fornix, and the corpus callosum, ad-hoc analysis was applied to AD and RD; the first component is an indicator for axonal degradation and degeneration and the second one for demyelination.[32,33] In the posterior part of the cingulum, the means of the RD were increased by 11.4% at the end of RT ($p < 0.001$) and by 10.5% 1-month post-RT from pre-RT ($p < 0.008$), while the means in the AD were not changed significantly at both time points, suggesting the radiation-induced demyelination is predominant. Similarly, in the fornix, the means of the RD were increased by 7.1% at the end

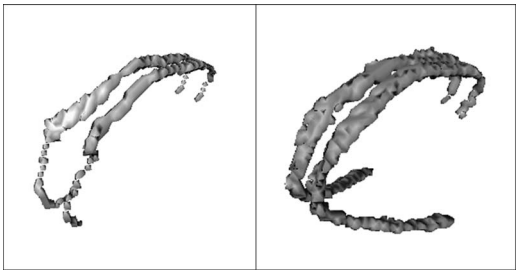

FIG. 7. A comparison between the results obtained by our proposed method (right) and the method reported by Wakana (Ref. 14) (left). Note that Wakana's method reconstructed a small number of fibers and thus underestimated the structure cross section. Also, it did not reconstruct the posterior left and right parts.

TABLE II. The absolute value of the mean and the estimation standard error for diffusion indices in pre-RT and the percentage changes in the mean, the estimation standard error, and the *t*-test *p*-value of the percentage changes in end-RT and 1-month post-RT with respect to pre-RT.

		Pre-RT			End-RT			1-month post-RT		
		Mean	SE of Mean		Mean	SE of Mean	*p*-value	Mean	SE of Mean	*p*-value
Cg_P	FA	0.395	8.72×10^{-3}	%ΔFA	− 14.0%	1.68%	0.000	− 11.9%	1.60%	0.000
	MD	6.60×10^{-6}	1.17×10^{-7}	%ΔMD	6.5%	1.07%	0.000	6.3%	1.95%	0.008
Cg_S	FA	0.430	5.60×10^{-3}	%ΔFA	− 5.1%	1.62%	0.009	− 3.1%	1.15%	0.020
	MD	6.12×10^{-6}	6.06×10^{-8}	%ΔMD	1.2%	0.94%	0.245	0.0%	0.90%	0.999
Cg_A	FA	0.376	1.14×10^{-2}	%ΔFA	− 6.1%	3.03%	0.068	− 6.6%	1.90%	0.005
	MD	6.76×10^{-6}	1.30×10^{-7}	%ΔMD	1.1%	1.88%	0.565	1.7%	1.06%	0.128
Fx	FA	0.335	9.03×10^{-3}	%ΔFA	− 12.5%	1.45%	0.000	− 12.8%	2.08%	0.000
	MD	1.25×10^{-5}	2.86×10^{-7}	%ΔMD	4.5%	1.67%	0.021	2.4%	1.61%	0.171
CC	FA	0.743	7.56×10^{-3}	%ΔFA	− 5.2%	0.76%	0.000	− 6.4%	0.60%	0.000
	MD	6.40×10^{-6}	7.69×10^{-8}	%ΔMD	6.8%	0.92%	0.000	8.5%	1.11%	0.000

An index with *p*-value <0.005 is considered significant. Cg: cingulum; CC: corpus callosum; Fx: fornix. The letters P, S, and A denote the posterior, superior, and anterior, respectively.

of RT ($p = 0.005$) and by 4.9% 1-month post-RT ($p = 0.04$) from pre-RT, while the means of the AD were changed neither substantially nor significantly at both time points. However, in the corpus callosum, the means of both RD and AD were increased significantly at the end of RT and 1-month post-RT from pre-RT. The means of RD were increased significantly by 17.0% ($p < 0.001$) at the end of RT and to 21.8% 1-month post-RT. The increases in the mean AD, although statistically significant, were in a much smaller extent, as 2.4% ($p = 0.001$) and 2.6% ($p = 0.01$) at the end of RT and 1-month post-RT, respectively, indicating that radiation effects on the corpus callosum are predominantly demyelination.

III.C.2. Comparing the structures through the percentage changes in diffusion indices

We applied rigorous analysis to determine whether there were significantly different radiation effects on these extracted structures by comparing different cingulum parts (posterior versus superior, superior versus anterior, and posterior versus anterior), the cingulum versus the fornix, the cingulum versus the corpus callosum, and the fornix versus the corpus callosum through the mean FA and MD percentage changes from pre-RT to end-RT and to 1-month post-RT (Fig. 8 and Table III). As can be understood from Table III, at the end-RT and 1-month post-RT, there were significant differences between the cingulum's posterior and superior parts in terms of percentage changes in both the mean FA and MD, between the corpus callosum and the fornix in terms of percentage changes of the mean FA, and between the corpus callosum and the cingulum in terms of percentage changes of the mean MD. Moreover, despite the absolute values of their diffusion indices, their percentage changes were not significantly different in the superior and anterior parts of the cingulum. Furthermore, the cingulum and fornix were not significantly different, but they were both significantly different from the corpus callosum in terms of the percentage changes of diffusion indices.

IV. DISCUSSION

In this study, we automatically segmented the entire corpus callosum, almost the entire cingulum fiber bundle and most parts of the body and crura of the fornix by applying the newly proposed segmentation methods. We showed the high reproducibility of the proposed algorithm for segmenting the cingulum of the test–retest NBIA data, which is essential for the longitudinal investigation of the radiation effect on the fiber bundle. Statistical analysis of the extracted structures supports that whole brain radiation therapy similarly affects the posterior part of the cingulum and the fornix, two important fiber tracts in the limbic circuit, as demyelination is the predominant effect. Moreover, radiation affects the anterior and superior parts of the cingulum in a much smaller and nonsignificant degree. Our findings suggest that different white matter fibers have different sensitivity to radiation, which may contribute to the selective cognitive dysfunction in memory and learning function after brain irradiation, as the early change in a DTI index of the posterior cingulum associated with the decline in memory function 18 months after RT is shown in a previous study.[10] To further understand the response of white matter fiber bundles to radiation, associated cognitive function outcomes and thereby sparing the critical functional anatomic structures in clinical trials, it is important to develop sophisticated, automated and reliable segmentation algorithms for delineation of the white matter structures, particularly for the small fiber bundles.

The high Dice coefficients of the segmented cingulum structures for the test–retest NBIA data demonstrate a high level of reproducibility for the proposed algorithm. Moreover, the low reproducibility coefficients of the diffusion indices in the cingulum posterior and superior parts (RC(FA) < 6.5% and RC(MD) < 4.3%) allow us to detect a small degree of the changes with significant confidence. It should be mentioned that the imperfect coregistration of the test and retest images also contributes to the Dice coefficient, as well as to the within-subject variance of the diffusion indices, especially in smaller structures such as the cingulum anterior part. Comparing the performance of the proposed method

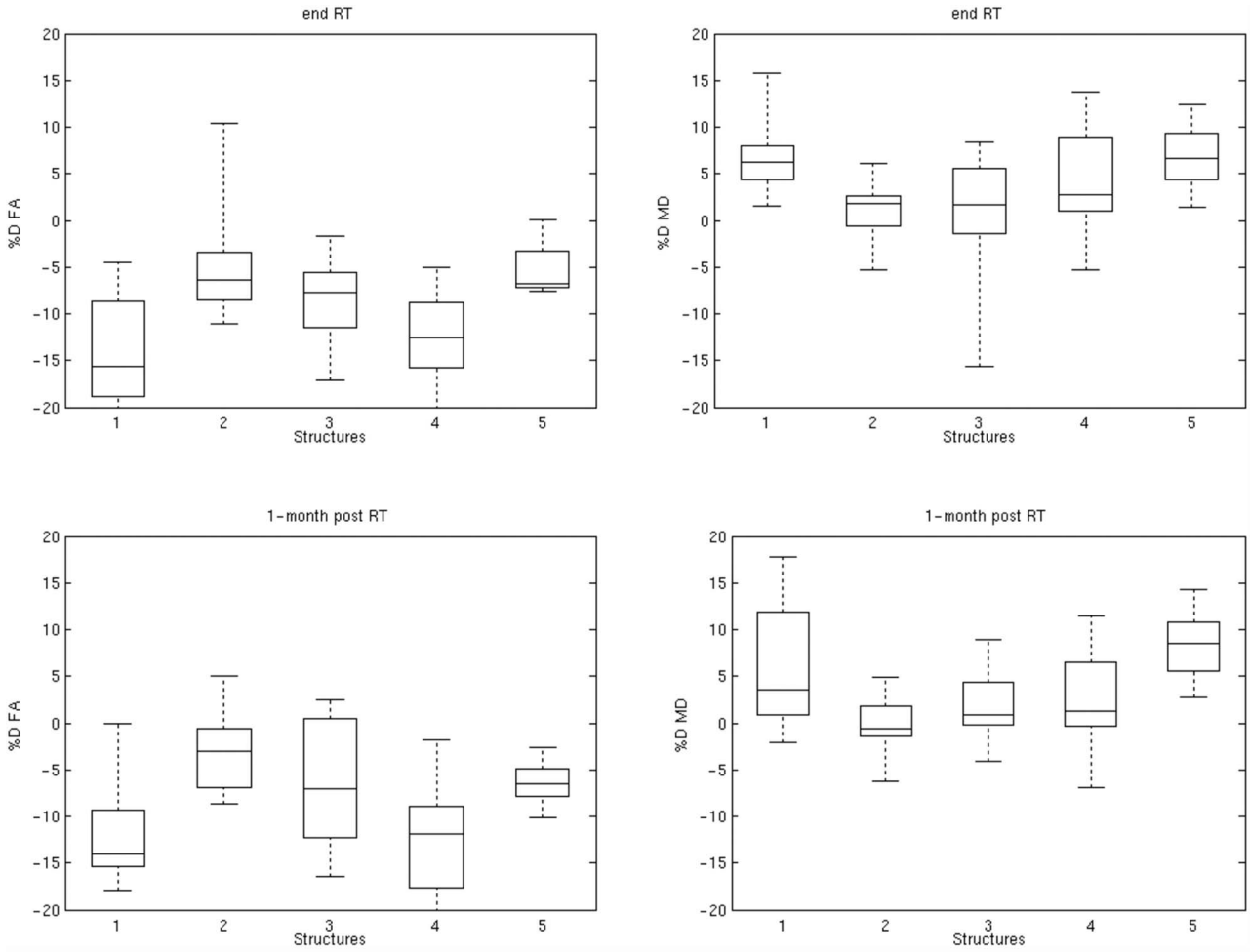

FIG. 8. Comparing percentage changes in the mean FA and MD in end-RT (top) and 1-month post-RT (bottom) with respect to pre-RT in different structures. The numbers 1–5 represent the posterior, superior, and anterior parts of the cingulum, the fornix, and the corpus callosum, respectively. The central marks are the median, the edges of the boxes are the 25th and 75th percentiles, and the whiskers extend to the most extreme data points.

and the tractography followed by ROIs insertion method by Wakana *et al.*[14] suggests that our method *works* superior to theirs in estimating the local thickness of the structure more precisely and in reconstructing the posterior parts more completely.

To analyze the effects of radiation on the various white matter fiber bundles, a region of interest drawn within the white matter structure and a manual contour of the fiber bundle have been used previously.[7,8] Automated fiber tractography and segmentation methods, on the other hand, are much more desirable and can improve the reproducibility of the delineated structures and possibly the accuracy. However, different geometrical shapes and diffusion characteristics in the different fiber tracts require us to adopt different strategies for their segmentation. In some parts of the cingulum such as the anterior part and the joint segment between the superior and posterior parts, sometimes a low anisotropy index is seen. This may lead to a discontinuity in segmenting the fiber tract by a front propagation based on local diffusion characteristics. Manipulating the threshold on the similarity measure (which is in charge of the front propagation) to get the front to propagate within the tract, compromises the segmentation specificity by penetrating into some other structures in the neighborhood of the cingulum. Tractography, on the other hand, can propagate a fiber (a front with 1-voxel local thickness) in its axial direction (parallel to the fiber

TABLE III. Comparing different structures by *t*-test *p*-value on the percentage changes in diffusion indices.

		Cg P vs Cg S	Cg S vs Cg A	Cg P vs Cg A	Cg vs Fx	Cg vs CC	Fx vs CC
End-RT	*p*-value of %ΔFA	0.001	0.775	0.033	0.036	0.025	0.000
	p-value of %ΔMD	0.001	0.985	0.021	0.418	0.008	0.237
1-month post-RT	*p*-value of %ΔFA	0.000	0.132	0.044	0.022	0.461	0.007
	p-value of %ΔMD	0.008	0.223	0.054	0.870	0.001	0.005

P-value assigned to the percentage changes in the mean FA and MD in end-RT (top) and 1-month post-RT (bottom) with respect to pre-RT. Cg: cingulum; CC: corpus callosum; Fx: fornix. The letters P, S, and A denote the posterior, superior, and anterior, respectively.

main axis) inside the low-anisotropy regions of the fiber tract of interest, without propagating into irrelevant structures. The advantage of a tractography algorithm over a segmentation algorithm is that it is less sensitive to the fractional anisotropy threshold; however, one should also be aware of erroneous or uncertain trajectories.

Using tractography to reconstruct the whole structure of a long fiber tract with a large local thickness variation like the cingulum, one must use a large number of closely inserted ROIs along the tract. However, a manual depiction of such a large number of ROIs is *undoubtedly* time consuming. Therefore, we introduced a seed-based tractography for segmenting the entire cingulum fiber tract, which dramatically reduces the operator's interaction time and effort. Moreover, by running the fibers between the closely inserted ROIs, there is no need to control the angle between two successive line segments in the FACT tractography algorithm.[29]

Compared to the cingulum, the signal-to-noise ratio of the diffusion measurements on the fornix is low, which leads to a low anisotropy index and noisy directionality. Moreover, there are more branching fibers from the fornix body. Despite these challenging issues, given that the structure is relatively small, manual insertion of the ROI is still feasible. For these reasons, we performed regular multiple ROIs tractography to segment this fiber tract. However, we adopted a different ROI depiction scheme to simultaneously gain a high level of segmentation sensitivity and specificity. The fornix is divided into three anatomical regions: posterior, body, and anterior parts. The fornix originates posteriorly as efferent fibers from the hippocampus composing the fimbria, which then form the crus of the fornix. The fibers from the left and right hemispheres joining in the midline of the brain form the body of the fornix, which runs anteriorly between the lateral ventricles. The anterior region of the fornix again separates into right and left columns of the fornix, and the fibers terminate in several regions including the mamillary body, lateral and anterior nuclei of the thalamus, septal nucleus, and anterior part of the hypothalamus. In the current study, because of the low resolution of diffusion images, low diffusion signal in the anterior part, and a high amount of branching fiber tracts in the posterior part, only the fornix body and the posterior part up to the hippocampus are extracted. Therefore, the current assessment of radiation effect on the fornix does not reflect the characteristics of the whole fiber structure. It does not still rule out that the different anatomical or functional regions of the fornix respond to radiation differently.

Diffusion indices vary greatly from large to small white matter fiber bundles due to different axon architectures and different degrees of myelination. Also, in the same structure, different patients may have different diffusion indices at the baseline. Given that we are only interested in investigating changes of the diffusion indices in the white matter structures after irradiation and comparing the radiation effects on the different structures, using the percentage changes in the diffusion indices from pre-RT to end-RT and 1-month post-RT can minimize the effects of the intersubject and interstructure baseline variations on the results and make the comparison between the structures meaningful.

Radiation appears to affect different white matter fiber structures differently, as suggested by selective late cognitive dysfunctions.[7,10,35] WBRT, as a commonly used treatment modality for brain metastases, provides a platform to investigate this question. In this study, we focused on the two fiber tracts in the limbic circuit, which are efferent and afferent connections to the hippocampus, and compared the radiation effects on them with the corpus callosum, the largest white matter fiber bundle in the brain. Among the structures under study, the posterior cingulum part, fornix, and corpus callosum are the most radiation-sensitive structures by substantial percentage decreases in the fractional anisotropy and percentage increases in the radial diffusivity. Our analysis of the axial and radial diffusivities reveals that demyelination is the predominant radiation effect on the structures. A mild but statistically significant change in the axial diffusivity is observed only in the corpus callosum. However, since it is in a small extent, it may not be clinically significant. Whether this minor subacute increase in the axonal diffusivity in the corpus callosum is associated with axonal degradation or is progressive months or years after whole brain irradiation needs to be further investigated. A previous report on the radiation effect in patients received partial brain radiation, however, shows progressive increases, significantly in the radial diffusivity but nonsignificantly and to a small extent in the axial diffusivity, in the genu and splenium of the corpus callosum up to 45 weeks after starting RT.[7] Also, a previous study reports progressive changes in both the radial and axial diffusivities in the posterior part of the cingulum up to 6 months after RT in patients treated by partial brain radiation and the early change in the DTI index associated with memory function decline 18 months post-RT.[10] Our understanding of the factors that affect the change in the axial diffusivity positively or negatively after irradiation is limited and requires for further studies.

Although axial diffusivity and radial diffusivity are indicators for axonal degradation/degeneration and demyelination, respectively,[32,33] one should be cautious of direct association of the changes in these two indices with the changes in underlying tissue structures. The special cases are fiber crossing in complex tissue structures and misregistration.[36] In our study, we evaluated the registration performance before data processing. In addition, the fiber bundles under the study do not have major crossing areas compared to their total volumes. Therefore, the radial diffusivity change observed in this study is unlikely due to misregistration and fiber crossing.

In the current study of the patients received whole brain RT, the percentage changes in FA and RD of the posterior cingulum 1 month post-RT are greater than the changes in the patients received partial brain radiation 6 months post-RT

In the current study of patients received whole brain RT, percentage changes in the DTI indices of the posterior cingulum 1 month post-RT are greater than changes in the patients received partial brain radiation 6 months post-RT,[10] supporting the concept that the whole brain RT affects the brain white matters more than the partial brain RT. Furthermore, substantial cognitive dysfunction, especially in memory function, 4–6 months following WBRT has been reported.[34] In this study, we developed computer-aided segmentation tools in

order to facilitate the study of the association of radiation damage of white matter structures with cognitive function decline following RT, and to avoid damage to critical structures.

V. CONCLUSION

To assess the effects of radiation therapy on the white matter fiber tracts of the limbic circuit, a seed-based tractography of the cingulum and a ROI-based segmentation of the fornix were proposed. By segmenting the two fiber tracts along with the corpus callosum, quantitative analysis of diffusion indices of the structures from pre- to post-RT indicates that the posterior segment of the cingulum, fornix and corpus callosum are highly susceptible to radiation-induced demyelination.

ACKNOWLEDGMENT

This work was supported in part by National Institutes of Health Grant Nos. RO1 NS064973 and 3 PO1 CA59827.

[a]Author to whom correspondence should be addressed. Electronic mail: mnazemza@umich.edu; Telephone: (734) 936-3358; Fax: (734) 936-2261.
[b]Electronic mail: chchap@umich.edu
[c]Electronic mail: tsl@med.umich.edu
[d]Electronic mail: ctsien@med.umich.edu
[e]Electronic mail: yuecao@umich.edu

[1]J. Bernier, E. J. Hall, and A. Giaccia, "Radiation oncology: A century of achievements," Nat. Rev. Cancer **4**(9), 737–747 (2004).
[2]W. Calvo, J. W. Hopewell, H. S. Reinhold, and T. K. Yeung, "Time- and dose-related changes in the white matter of the rat brain after single doses of X rays," Br. J. Radiol. **61**(731), 1043–1052 (1988).
[3]P. Monro and W. G. Mair, "Radiation effects on the human central nervous system 14 weeks after x-radiation," Acta Neuropathol. (Berl) **11**(4), 267–274 (1968).
[4]J. P. Glass, T. L. Hwang, M. E. Leavens, and H. I. Libshitz, "Cerebral radiation necrosis following treatment of extracranial malignancies," Cancer **54**(9), 1966–1972 (1984).
[5]G. E. Sheline, W. M. Wara, and V. Smith, "Therapeutic irradiation and brain injury," Int. J. Radiat. Oncol., Biol., Phys. **6**(9), 1215–1228 (1980).
[6]P. C. Sundgren and Y. Cao, "Brain irradiation: Effects on normal brain parenchyma and radiation injury," Neuroimaging Clin. N. Am. **19**(4), 657–668 (2009).
[7]V. Nagesh, C. I. Tsien, T. L. Chenevert, B. D. Ross, T. S. Lawrence, L. Junick, and Y. Cao, "Radiation-induced changes in normal appearing white matter in patients with cerebral tumors: A diffusion tensor imaging study," Int. J. Radiat. Oncol., Biol., Phys. **70**(4), 1002–1010 (2008).
[8]D. J. Mabbott, M. D. Noseworthy, E. Bouffet, C. Rockel, and S. Laughlin, "Diffusion tensor imaging of white matter after cranial radiation in children for medulloblastoma: Correlation with IQ," Neuro-oncology **8**(3), 244–252 (2006).
[9]T. C. Chua, W. Wen, X. Chen, N. Kochan, M. J. Slavin, J. N. Trollor, H. Brodaty, and P. S. Sachdev, "Diffusion tensor imaging of the posterior cingulate is a useful biomarker of mild cognitive impairment," Am. J. Geriatr. Psychiatry **17**(7), 602–613 (2009).
[10]C. H. Chapman, V. Nagesh, P. Sundgren, H. Buchtel, T. L. Chenevert, L. Junck, T. S. Lawrence, C. I. Tsien, and Y. Cao, "Diffusion tensor imaging of normal-appearing white matter as biomarker for radiation-induced late delayed cognitive decline," Int. J. Radiat. Oncol., Biol., Phys. **82**(5), 2033–2040 (2012).
[11]A. Ghia, W. A. Tome, S. Thomas, G. Cannon, D. Khuntia, J. S. Kuo, and M. P. Mehta, "Distribution of brain metastases in relation to the hippocampus: Implications for neurocognitive functional preservation," Int. J. Radiat. Oncol., Biol., Phys. **68**(4), 971–977 (2007).
[12]O. K. Abayomi, "Pathogenesis of irradiation-induced cognitive dysfunction," Acta Oncol. **35**(6), 659–663 (1996).
[13]L. Concha, D. W. Gross, and C. Beaulieu, "Diffusion tensor tractography of the limbic system," AJNR Am. J. Neuroradiol. **26**(9), 2267–2274 (2005).
[14]S. Wakana, A. Caprihan, M. M. Panzenboeck, J. H. Fallon, M. Perry, R. L. Gollub, K. Hua, J. Zhang, H. Jiang, P. Dubey, A. Blitz, P. van Zijl, and S. Mori, "Reproducibility of quantitative tractography methods applied to cerebral white matter," NeuroImage **36**(3), 630–644 (2007).
[15]E. Heiervang, T. E. J. Behrens, C. E. Mackay, M. D. Robson, and H. Johansen-Berga, "Between session reproducibility and between subject variability of diffusion MR and tractography measures," NeuroImage **33**, 867–877 (2006).
[16]S. P. Awate, H. Zhang, and J. C. Gee, "A Fuzzy, nonparametric segmentation framework for DTI and MRI analysis: With applications to DTI-tract extraction," IEEE Trans. Med. Imaging **26**(11), 1525–1536 (2007).
[17]V. Mohan, G. Sundaramoorthi, and A. Tannenbaum, "Tubular surface segmentation for extracting anatomical structures from medical imagery," IEEE Trans. Med. imaging **29**(12), 1945–1958 (2010).
[18]J. Melonakos, V. Mohan, M. Niethammer, K. Smith, M. Kubicki, and A. Tannenbaum, "Finsler tractography for white matter connectivity analysis of the cingulum tract," *Medical Image Computing and Computer Assisted Intervention (MICCAI)* (2007), Vol. 4791, pp. 36–43.
[19]M. R. Nazem-Zadeh, E. Davoodi-Bojd, and H. Soltanian-Zadeh, "Level set fiber bundle segmentation using spherical harmonic coefficients," Comput. Med. Imaging Graph. **34**(3), 192–202 (2010).
[20]M. R. Nazem-Zadeh, E. Davoodi-Bojd, and H. Soltanian-Zadeh, "Atlas-based fiber tracts segmentation in the brain using spherical harmonic coefficients," NeuroImage **54**, 146–164 (2011).
[21]M. R. Nazem-Zadeh, K. Jafari-Khouzani, E. Davoodi-Bojd, Q. Jiang, and H. Soltanian-Zadeh, "Clustering method for estimating principal diffusion directions," NeuroImage **57**(3), 825–838 (2011).
[22]M. F. Abdul-Rahman, A. Qiu, and K. Sim, "Regionally specific white matter disruptions of fornix and cingulum in schizophrenia" PLoS ONE **6**(4), e18652 (2011).
[23]A. Stadlbauer, E. Salomonowitz, G. Strunk, T. Hammen, and O. Ganslandt, "Quantitative diffusion tensor fiber tracking of age-related changes in the limbic system," Eur. Radiol. **18**(1), 130–137 (2008).
[24]P. Perona and J. Malik, "Scale-space and edge detection using anisotropic diffusion," IEEE Trans. Pattern Anal. Mach. Intell. **12**(7), 629–639, (1990).
[25]G. Gerig, O. Kubler, R. Kikinis, and F. A. Jolesz, "Nonlinear anisotropic filtering of MRI data," IEEE Trans. Med. Imaging **11**(2), 221–232 (1992).
[26]S. Osher and J. Sethian, "Fronts propagating with curvature dependent speed: Algorithms based on Hamilton–Jacobi formulations," J. Comput. Phys. **79**, 12–49 (1988).
[27]S. Osher and N. Paragios, "Level set methods,'' in *Geometric Level Set Methods in Imaging, Vision, and Graphics* (Springer-Verlag, New York, 2003), pp. 3–20.
[28]I. M. Mitchell, "The flexible, extensible and efficient toolbox of level set methods," J. Sci. Comput. **35**(2–3), 300–329 (2008).
[29]S. Mori and P. C. van Zijl, "Fiber tracking: Principles and strategies—A technical review," NMR Biomed. **15**(7–8), 468–480 (2002).
[30]H. X. Barnhart and D. P. Barboriak, "Applications of the repeatability of quantitative imaging biomarkers: A review of statistical analysis of repeat data sets," Transl. Oncol. **2**, 231–235 (2009).
[31]M. R. Nazem-Zadeh, S. Saksena, A. Babajani-Fermi, Q. Jiang, H. Soltanian-Zadeh, M. Rosenblum, T. Mikkelsen, and R. Jain, "Segmentation of corpus callosum using diffusion tensor imaging: Validation in patients with glioblastoma," BMC Med. Imaging **12**(10), (2012).
[32]S. K. Song, S. W. Sun, W. K. Ju, S. J. Lin, A. H. Cross, and A. H. Neufeld, "Diffusion tensor imaging detects and differentiates axon and myelin degeneration in mouse optic nerve after retinal ischemia," NeuroImage **20**(3), 1714–1722 (2003).
[33]S. Wang, E. X. Wu, D. Qiu, L. H. Leung, H. F. Lau, and P. L. Khong, "Longitudinal diffusion tensor magnetic resonance imaging study of radiation-induced white matter damage in a rat model," Cancer Res. **69**(3), 1190–1198 (2009).
[34]E. L. Chang, J. S. Wefel, K. R. Hess, P. K. Allen, F. F. Lang, D. G. Kornguth, R. B. Arbuckle, J. M. Swint, A. S. Shiu, M. H. Maor, and C. A. Meyers, "Neurocognition in patients with brain metastases treated with radiosurgery or radiosurgery plus whole-brain irradiation: A randomised controlled trial," Lancet Oncol. **10**(11), 1037–1044 (2009).
[35]C. H. Chapman, M. R. Nazem-Zadeh, T. S. Lawrence, C. I. Tsien, and Y. Cao, "Regional variation of white matter radiation sensitivity: A tract based spatial statistics (TBSS) study," Int. J. Radiat. Oncol., Biol., Phys. **81**(2), 298 (2011).
[36]C. A. Wheeler-Kingshott and M. Cercignani, "About "axial" and "radial" diffusivities," Magn. Reson. Med. **61**(5), 1255–1260 (2009).